Supplementary Information

Enhancing irradiation tolerance and inducing superlubricity in MoS_2/W multilayer film exposed to atomic oxygen

This PDF file includes:

Figs. S1 to S28

Tables S1 to S5

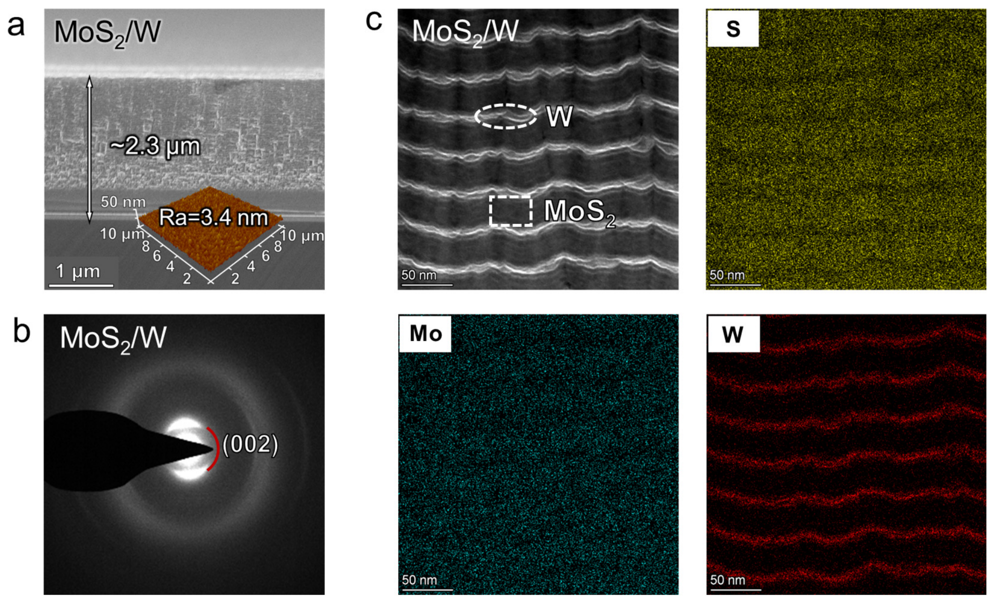

Fig. S1. Cross-sectional images of MoS_2/W multilayer film. a Thickness value and cross-sectional morphology of MoS_2/W multilayer film. Inset SPM image shows 3D morphology and roughness of the surface. **b** SAED pattern of MoS_2/W multilayer film. **c** HAADF-STEM and EDS mapping images of MoS_2/W multilayer film.

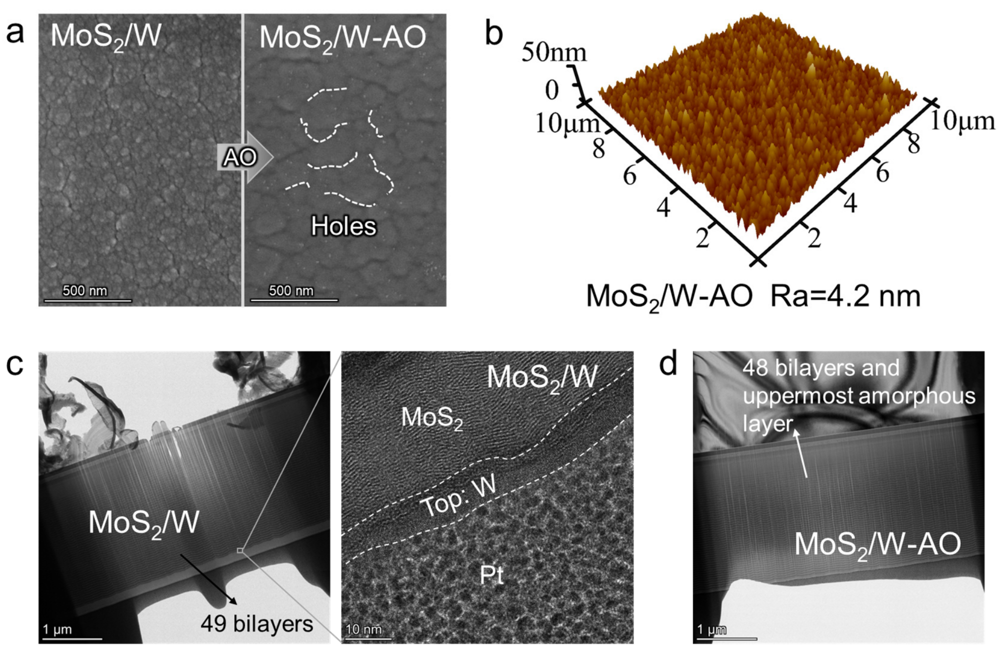

Fig. S2. Irradiation tolerance of MoS_2/W multilayer film. a Surface morphologies of the MoS_2/W multilayer film before and after AO irradiation with a total dose of 2.7×10^{21} atoms·cm^{-2}. **b** 3D morphology and roughness value of the MoS_2/W-AO multilayer film surface. **c** Cross-sectional TEM image and enlarged view of as-prepared MoS_2/W multilayer film (49 bilayers). **d** 48 bilayers and uppermost amorphous layer in the MoS_2/W-AO multilayer film.

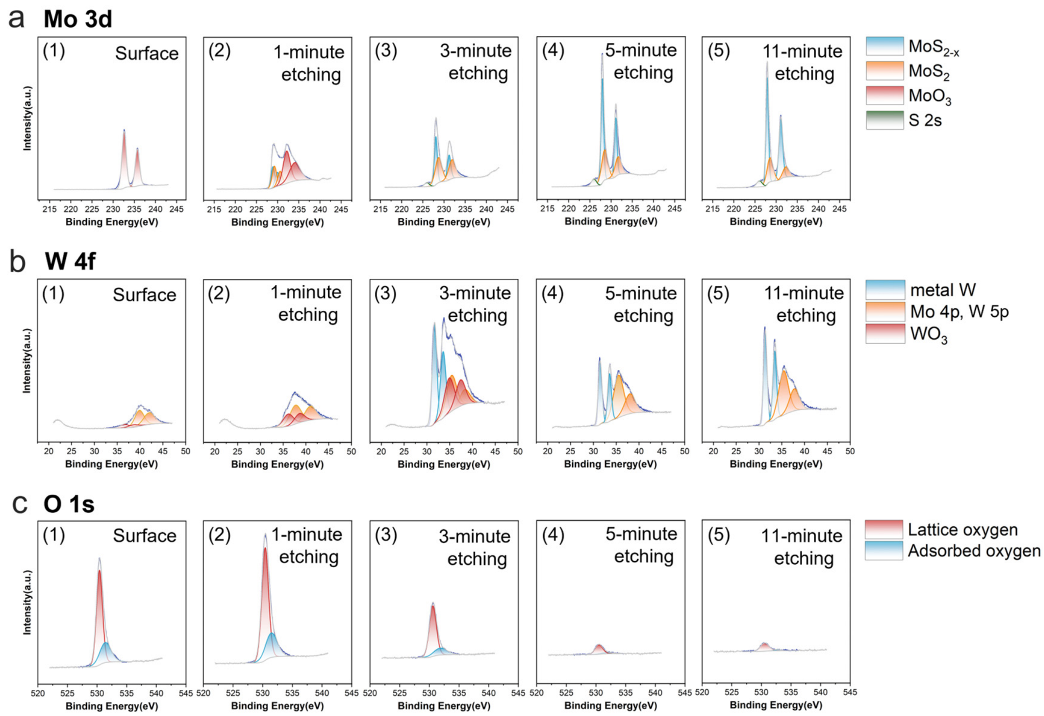

Fig. S3. XPS spectra of Mo 3d (a), W 4f (b), and O 1s (c) of the MoS_2/W-AO multilayer film at cumulative etching durations of 0, 1, 3, 5, and 11 minutes under a 5 keV argon ion beam[18,28]. All the spectra were fitted with the non-linear least square fit program using Gauss-Lorentzian peak shapes. As shown in (**a1-a2**), the double peaks at 232.1 and 235.0 eV are related to MoO_3. Moreover, the characteristic peaks (**a3-a5**) at 227.9 eV and 231.0 eV correspond to the Mo $3d_{5/2}$ and Mo $3d_{3/2}$ of MoS_{2-x}, another doublet peaks located at 228.6 eV and 231.7 eV are attributed to the Mo $3d_{5/2}$ and Mo $3d_{3/2}$ of MoS_2, and the small hump at ~225.9 eV is closely related to the S 2s peak. For (**b**), the double peaks at 35.6 eV and 37.8 eV belong to W $4f_{7/2}$ and W $4f_{5/2}$ of WO_3, and the peaks at 31.6 and 33.7 eV are related to W $4f_{7/2}$ and W $4f_{5/2}$ of metal W. In addition, the peaks at 35.9-41.9 eV are related to Mo 4p and W 5p, respectively. Figure (**c**) shows that two peaks centered at ~530.5 eV and ~532.1 eV are attributed to lattice oxygen and surface adsorbed oxygen, respectively.

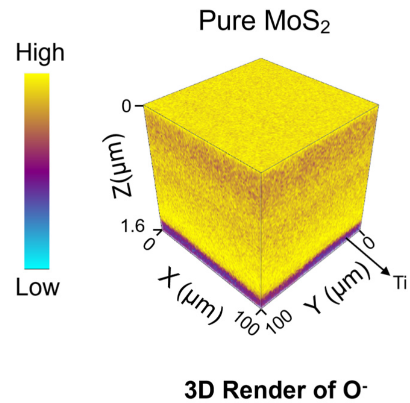

Fig. S4. 3D ToF-SIMS plot of O^- distribution (full depth) on pure MoS_2 film after 50 hours of AO irradiation. The vertical Z axis corresponds to the sample depth according to the irradiation time of the Cs^+ clusters beam.

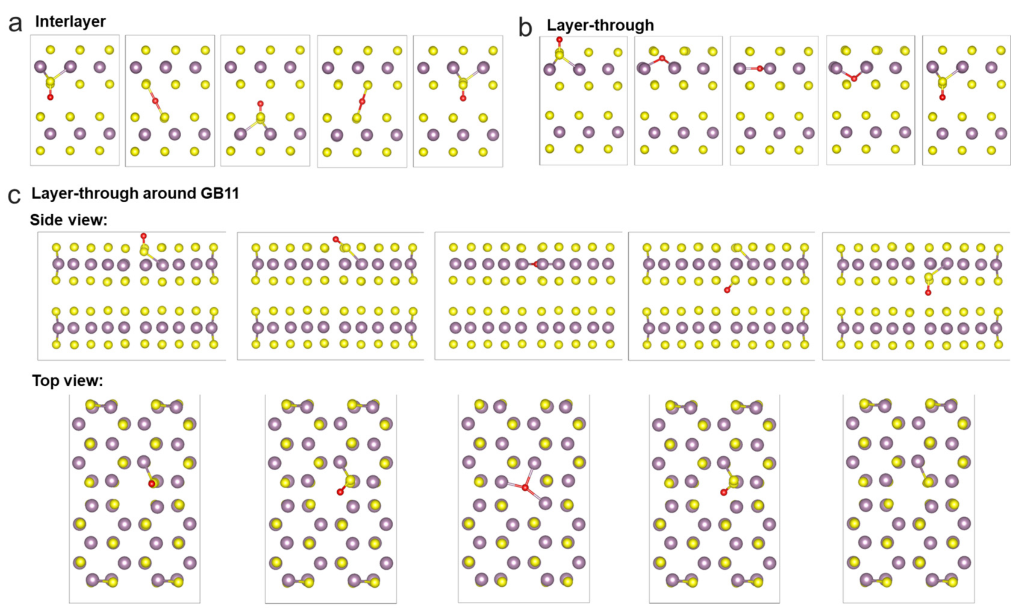

Fig. S5. The migration pathways of oxygen atoms in interlayer (a), through layer without (b), and with (c) grain boundaries (GB11) of MoS_2. Red, yellow, and brown balls represent oxygen atoms, sulfur atoms, and molybdenum atoms, respectively.

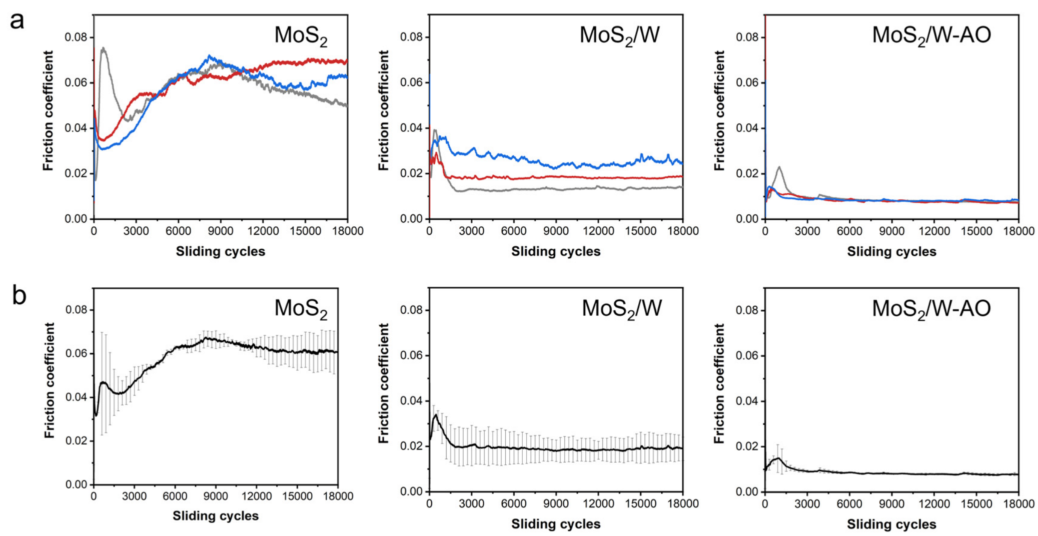

Fig. S6. Friction coefficient curves (a) and their average curves (b) for pure MoS_2, MoS_2/W, and MoS_2/W-AO multilayer films. Three repeated tribological experiments were carried out for each film. Skip points of the average curves: 3,000.

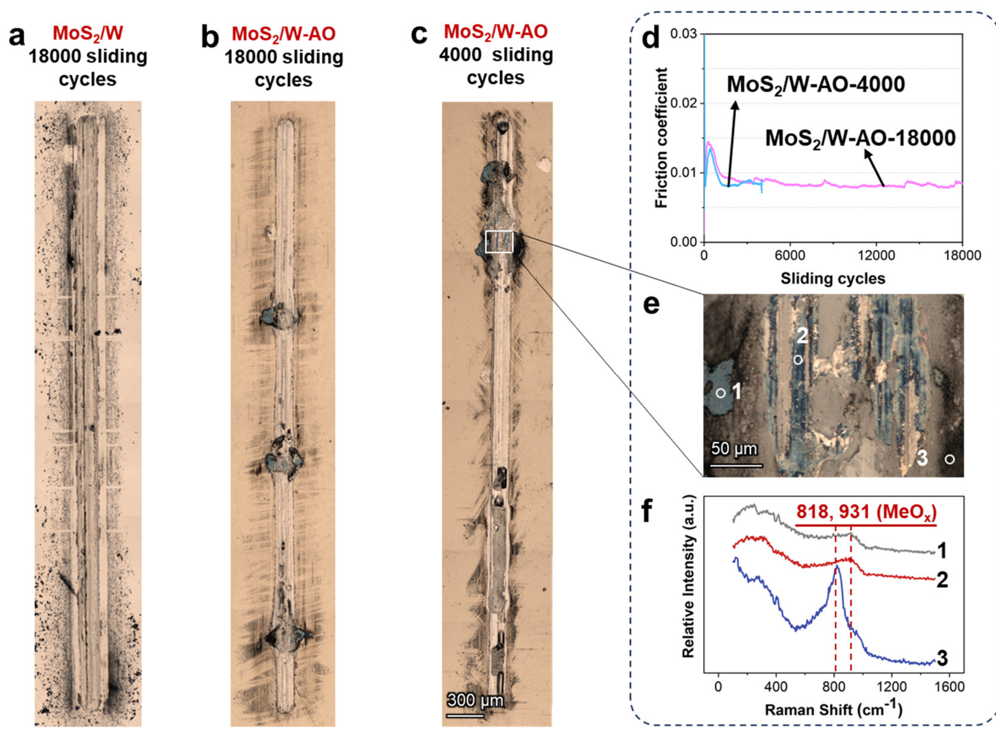

Fig. S7. Examinations of the wear tracks of MoS_2/W and MoS_2/W-AO multilayer films. a-c Full view of wear tracks under an optical microscope. The comparison of the wear track morphology before and after AO irradiation shows that the wear track of the MoS_2/W-AO multilayer film has significant heterogeneity. **d** The friction coefficient curve of the MoS_2/W-AO multilayer film after 4,000 sliding cycles basically matches that after 18,000 sliding cycles. **e** Enlarged view of the wear track of MoS_2/W-AO multilayer film after 4,000 sliding cycles. **f** Raman spectra collected from points 1, 2, and 3 on (**e**). Raman spectra show the existence of oxides in the sliding interface.

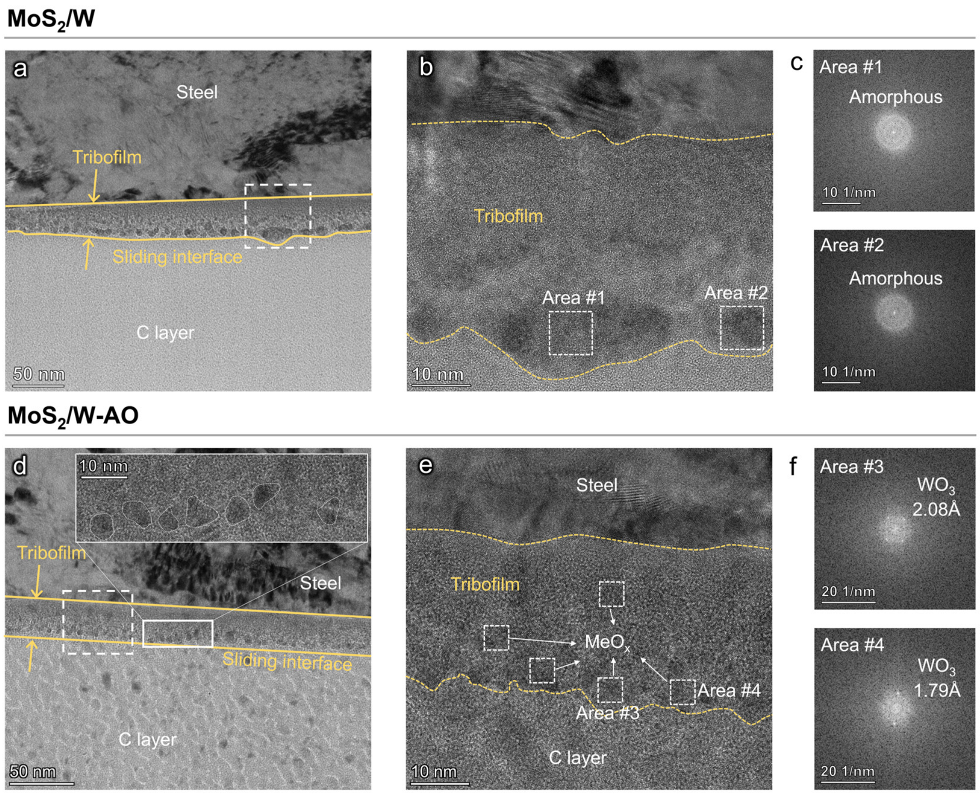

Fig. S8. Comparison of the tribofilms of the MoS_2/W and MoS_2/W-AO films. a Cross-sectional morphology of tribofilm for MoS_2/W multilayer film. **b** HRTEM image of the dashed square area in (**a**). **c** Fast Fourier transform images derived from Area #1 and #2 in (**b**). **d** Cross-sectional morphology of tribofilm for MoS_2/W-AO multilayer film. The inset is an enlarged view of the sliding interface. **e** HRTEM image of the dashed square area in (**d**). **f** Fast Fourier transform images derived from Area #3 and #4 in (**e**).

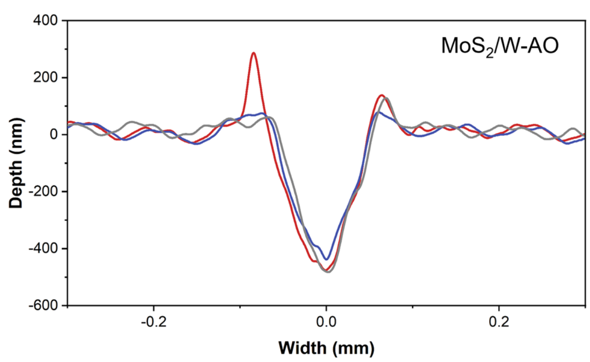

Fig. S9. Cross-sectional profiles of the MoS_2/W-AO multilayer film acquired after 18,000 sliding cycles in vacuum.

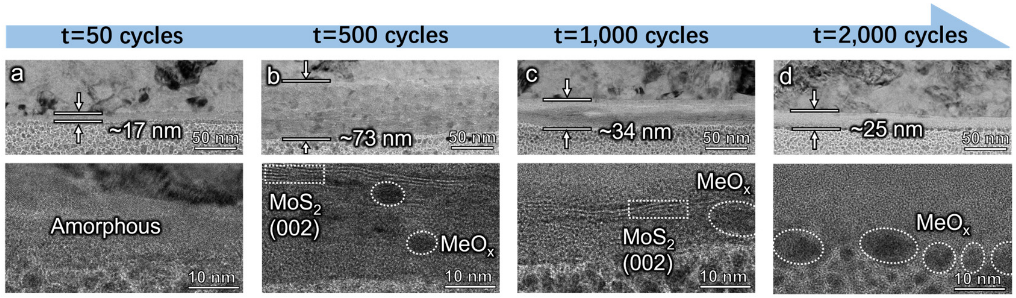

Fig. S10. The evolution mechanism of the tribofilm adhering to the counterpart ball surface of the MoS_2/W-AO multilayer film at 50 (a), 500 (b), 1,000 (c), and 2,000 (d) sliding cycles.

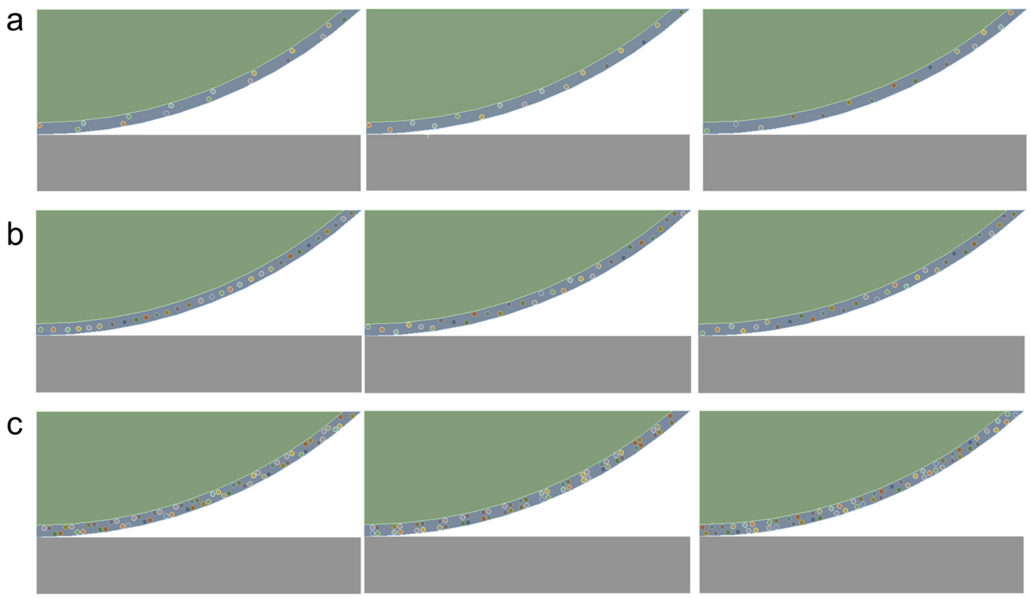

Fig. S11. Distribution diagrams of nanoparticles with concentrations of 7% (a), 14% (b), and 27% (c) used in the finite element simulation. Three different distributions for each concentration of nanoparticle were considered. The diameter of the nanoparticles is 10 nm in both models.

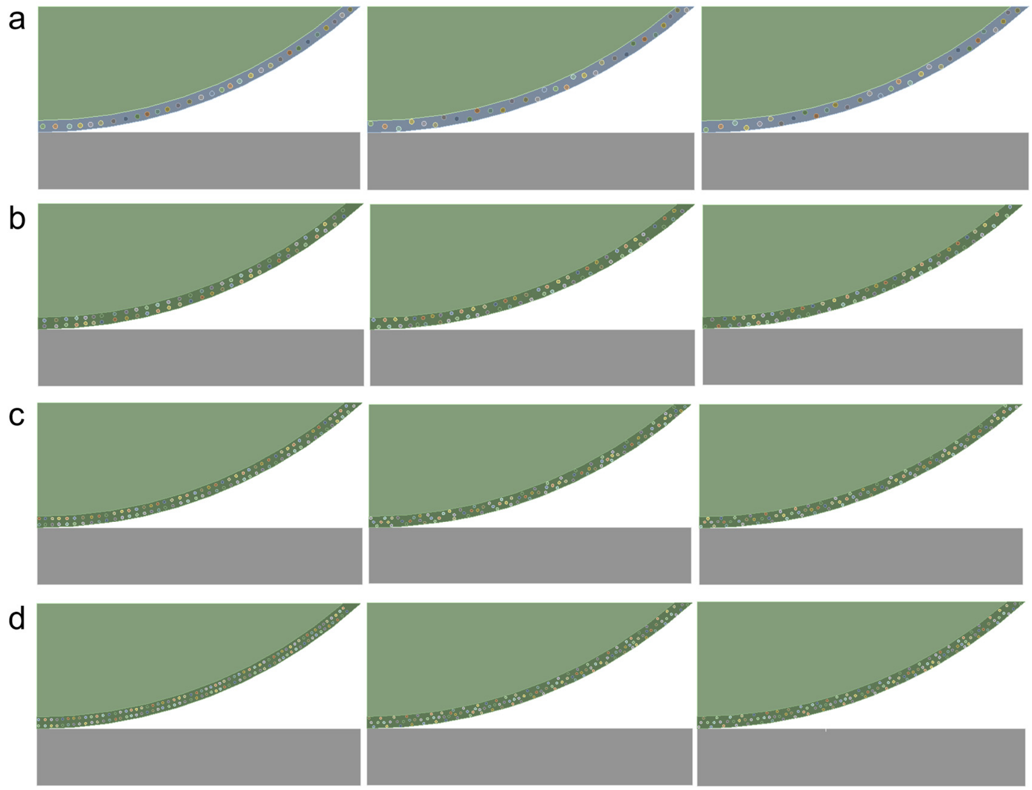

Fig. S12. Distribution diagrams of nanoparticles with diameters of 10.00 nm (a), 7.10 nm (b), 5.77 nm (c), and 5.00 nm (d) used in the finite element simulation. Three different distributions for each diameter of nanoparticle were considered. The concentration of the nanoparticles is 14% in both models.

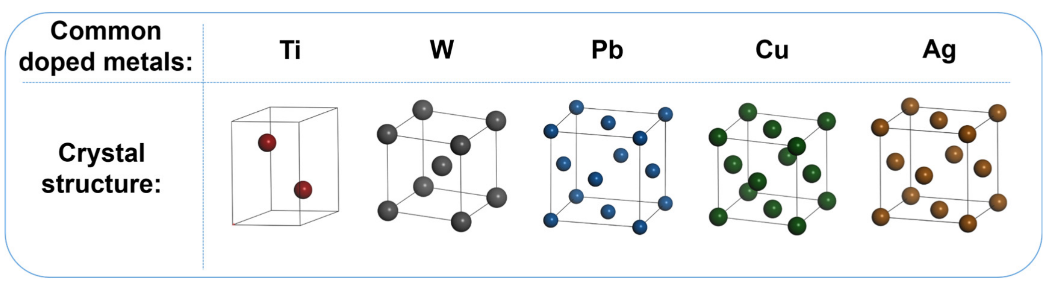

Fig. S13. Selection of metallic elements.

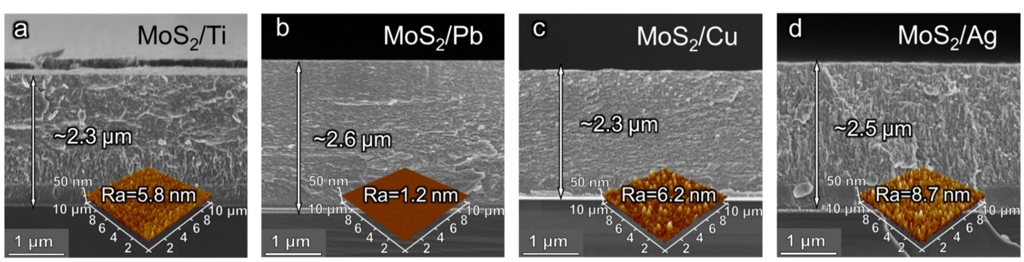

Fig. S14. Morphologies of MoS_2/Me films. Thickness values and cross-sectional morphologies of

MoS_2/Me films. Inset SPM images show 3D morphologies and roughness of the surfaces.

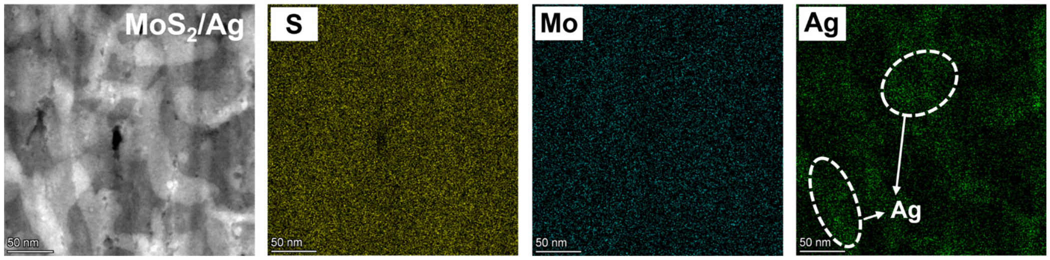

Fig. S15. Cross-sectional HAADF-STEM and EDS mapping images of the MoS_2/Ag composite film.

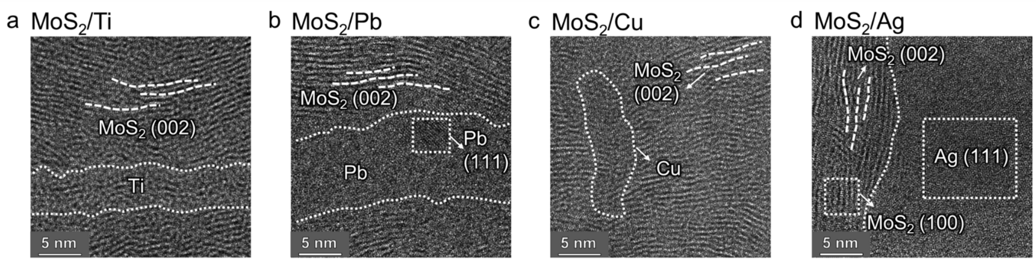

Fig. S16. HRTEM images of MoS_2/Me films.

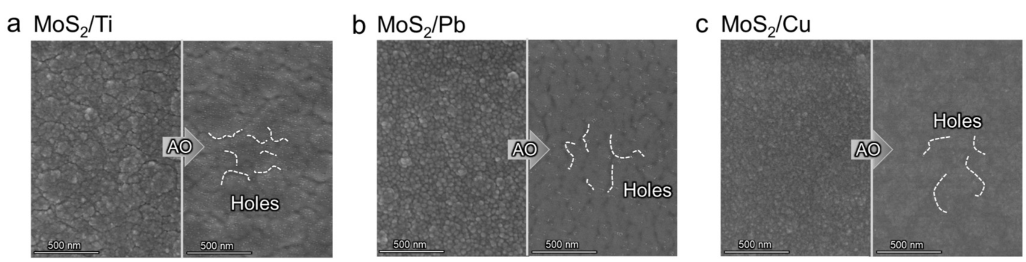

Fig. S17. Surface morphologies of the MoS_2/Ti (a), MoS_2/Pb (b), and MoS_2/Cu (c) multilayer films before and after AO irradiation with a total dose of 2.7×10^{21} atoms·cm^{-2}.

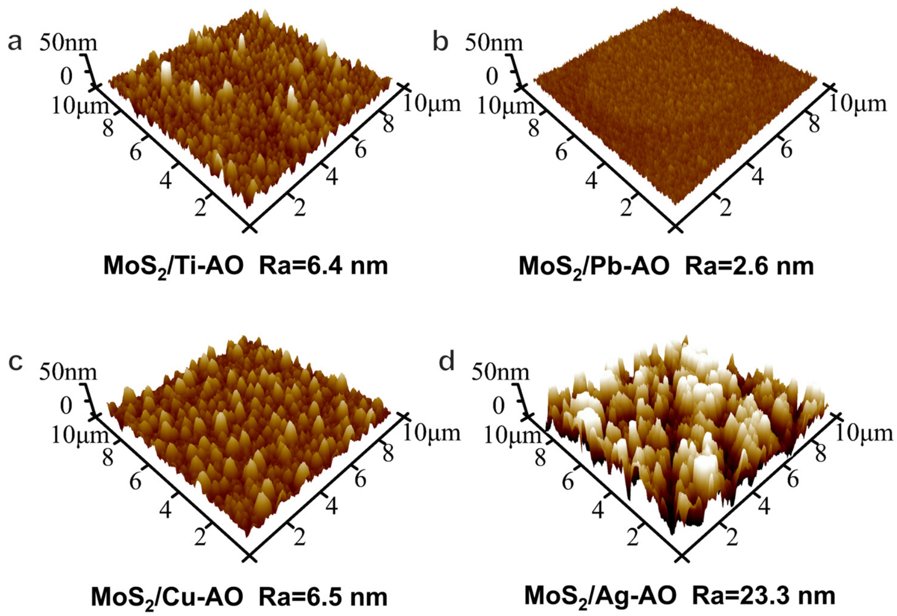

e

Ra	Unirradiated films (nm)	Irradiated films (nm)
MoS_2/W	3.4	4.2
MoS_2/Ti	5.8	6.4
MoS_2/Pb	1.2	2.6
MoS_2/Cu	6.2	6.5
MoS_2/Ag	8.7	23.3

Fig. S18. SPM images of the MoS_2/Me films. a-d 3D morphologies and roughness values of the MoS_2/Me-AO film surfaces. **e** Comparison of surface roughness before and after AO irradiation.

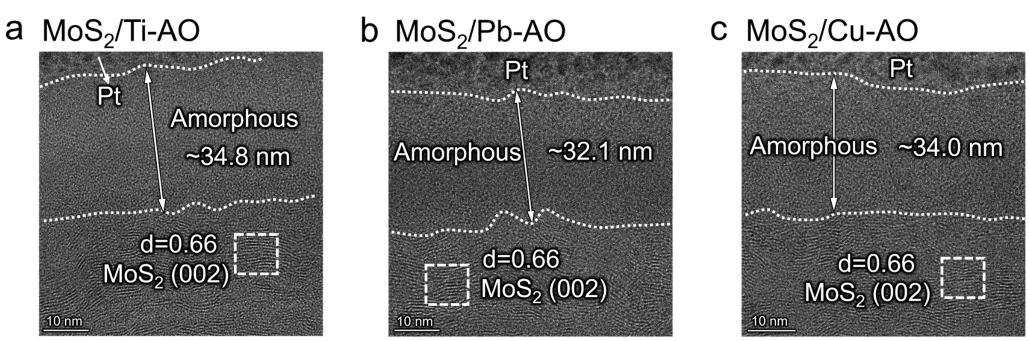

Fig. S19. Cross-sectional HRTEM images of the MoS_2/Ti-AO (a), MoS_2/Pb-AO (b), and MoS_2/Cu-AO (c) multilayer films.

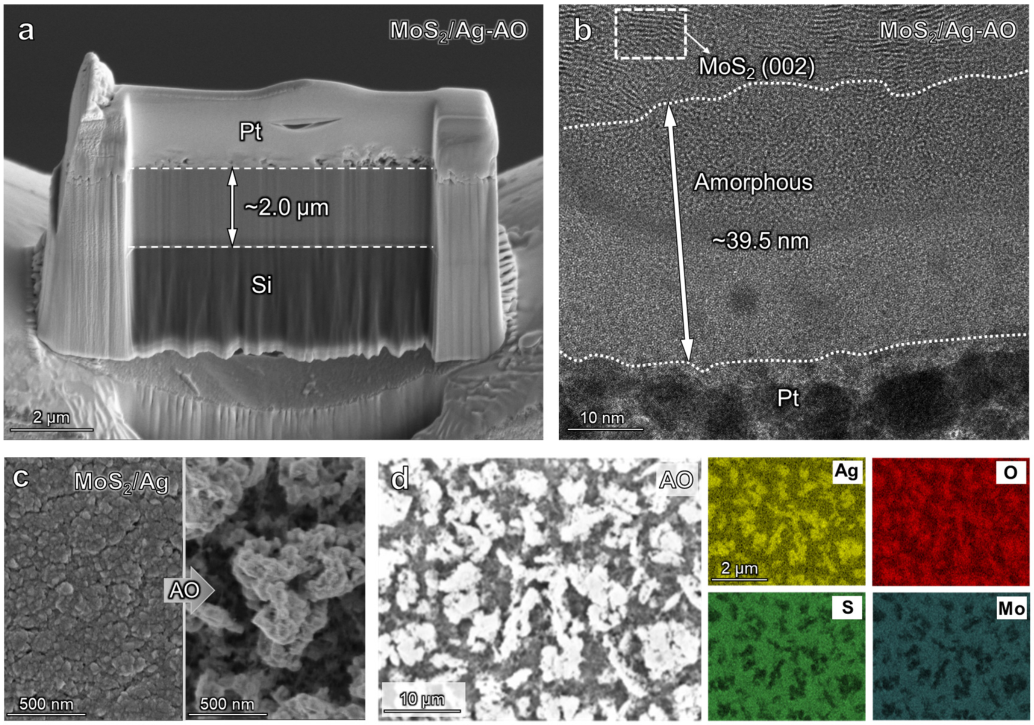

Fig. S20. Characterisation of the MoS_2/Ag composite film. a The thickness of the MoS_2/Ag-AO film obtained by the FIB technique. **b** Cross-sectional morphology of the MoS_2/Ag-AO film. **c** Surface morphologies of the MoS_2/Ag film before and after AO irradiation. Obviously, the surface of MoS_2/Ag-AO film is full of holes, showing serious damage. By comparing thicknesses before and after irradiation (**a** and Fig. S14d) and accounting for the amorphous layer's thickness (**b**), the oxidation depth of MoS_2/Ag film is ~539.5 nm. **d** HAADF-STEM and EDS mapping images of the MoS_2/Ag-AO film.

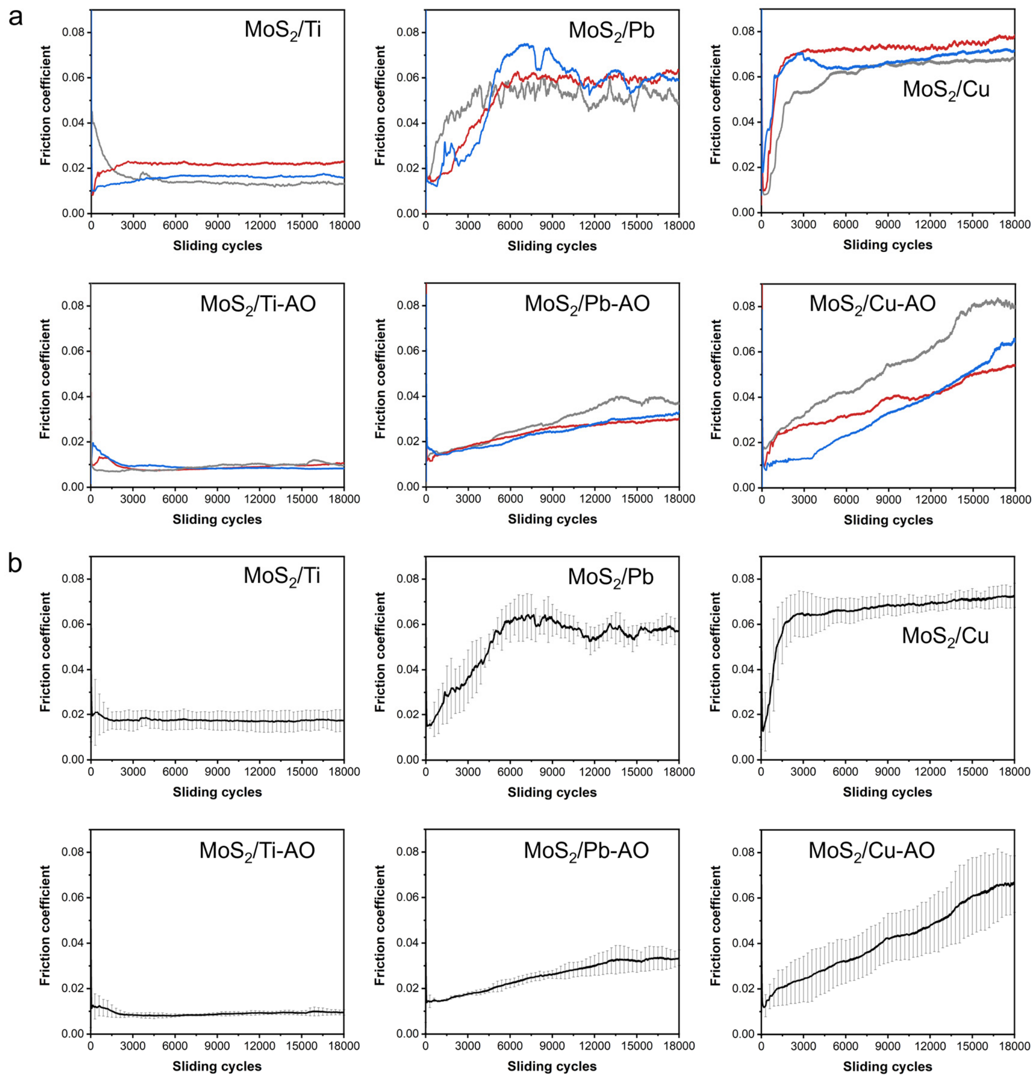

Fig. S21. Friction coefficient curves (a) and their average curves (b) for MoS_2/Me and MoS_2/Me-AO multilayer films. Three repeated tribological experiments were carried out for each film. Skip points of the average curves: 3,000.

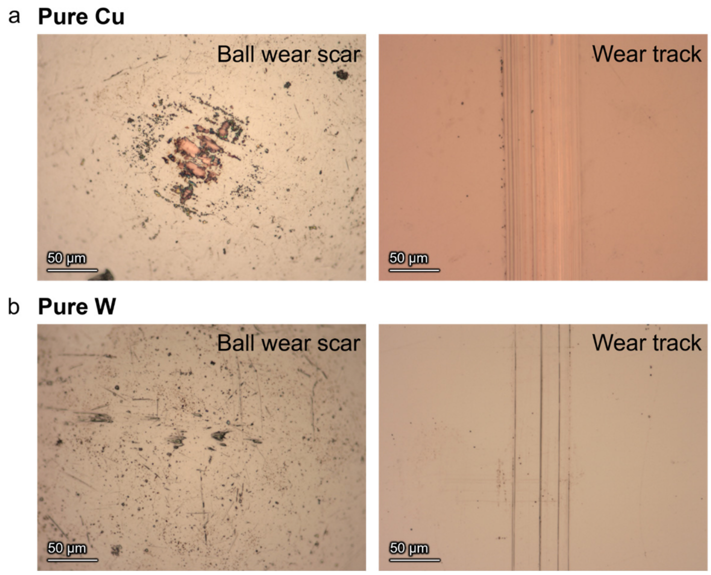

Fig. S22. Optical images of ball wear scars and wear tracks for pure metal films. a Cu adheres to the counterpart ball of the pure Cu film. **b** W can hardly adhere to the counterpart ball of the pure W film. The friction tests were carried out for 10 sliding cycles with a load of 1 N, a frequency of 1 Hz, an amplitude of 5 mm, and a vacuum pressure of less than 5×10^{-3} Pa.

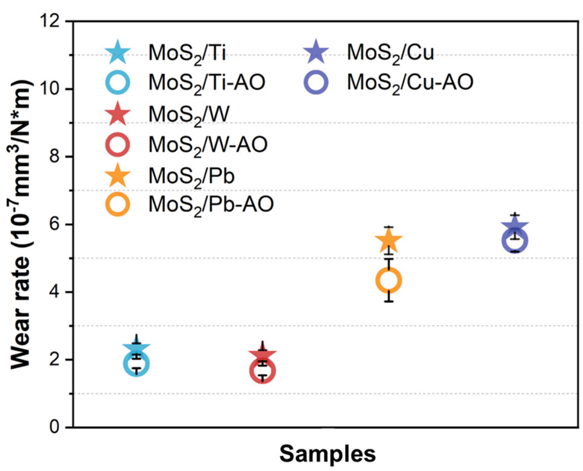

Fig. S23. Wear rates of MoS_2/Me and MoS_2/Me-AO films (18,000 sliding cycles).

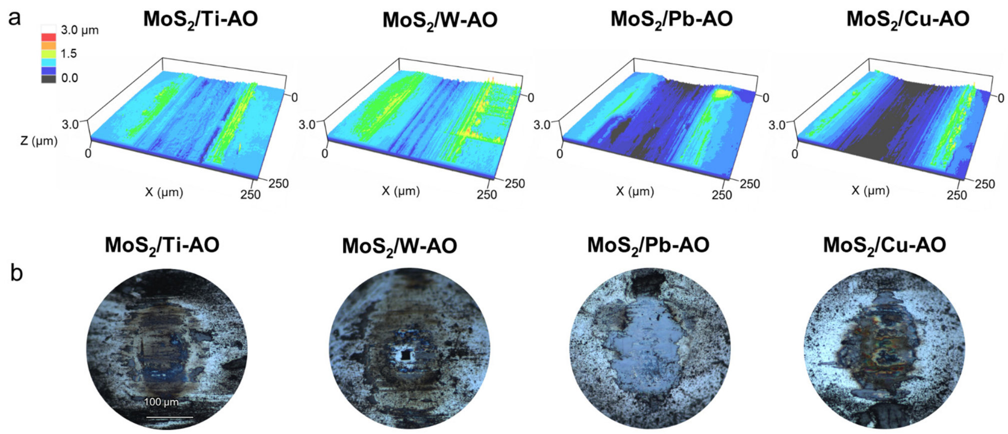

Fig. S24. Morphologies of wear tracks and ball wear scars for the MoS_2/Me-AO films after 18,000 sliding cycles. The hole in the ball wear scar of the MoS_2/W-AO originates from the FIB milling.

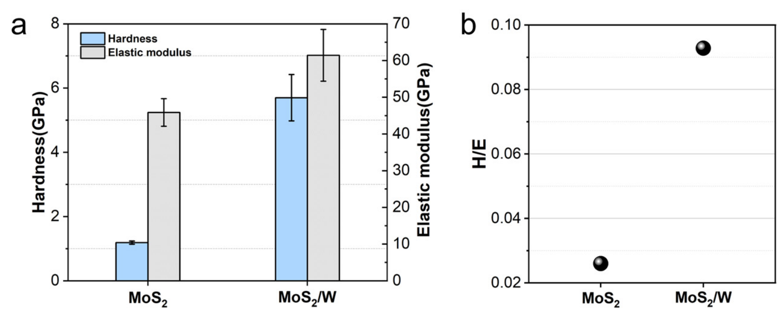

Fig. S25. Mechanical properties of as-prepared pure MoS_2 and MoS_2/W multilayer films. a-b Hardness, elastic modulus, and corresponding H/E of films.

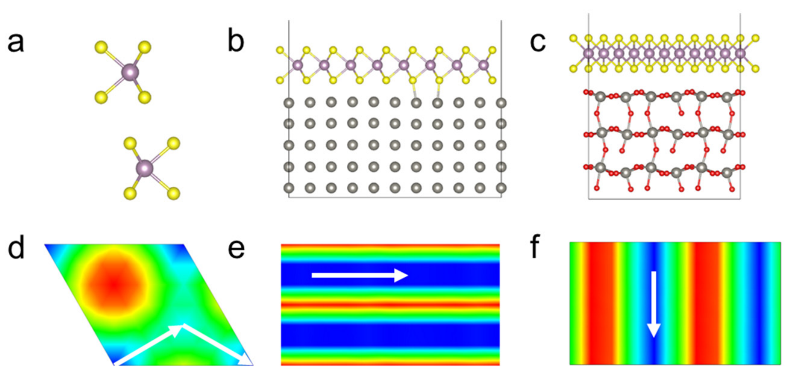

Fig. S26. The atomic configuration used to calculate friction of MoS_2/MoS_2 (a), MoS_2/W (b), and MoS_2/WO_3 (c) with LICP-FPHTC-Platform and the corresponding potential energy surfaces (d-f) obtained by calculation. Red, yellow, and brown balls represent oxygen atoms, sulfur atoms, and molybdenum atoms, respectively in (**a-c**). Blue represents low potential energy, red represents high potential energy in (**d-f**). The white arrow represents the optimal slip path, which is also the path applicable for friction calculation in the main text. Only the potential energy surfaces under a load of 1 GPa are illustrated here, and the morphology of the potential energy surface is the same under other loads studied in this paper.

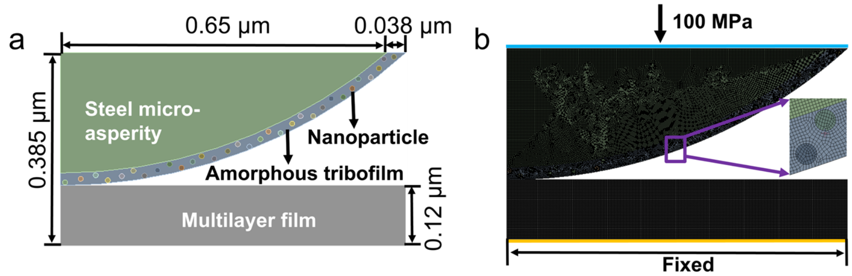

Fig. S27. Schematic diagram (a), mesh and boundary conditions (b) of finite element model.

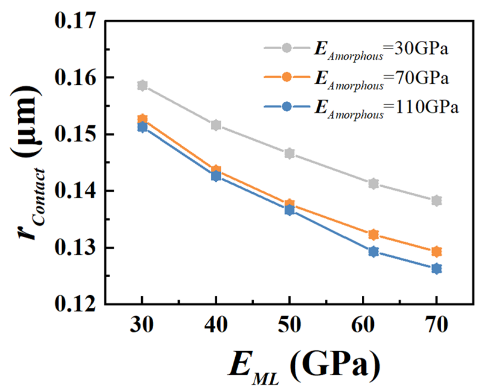

Fig. S28. The influence of elastic modulus $E_{Amorphous}$ of amorphous transfer film on contact radius $r_{Contact}$. The varying $E_{Amorphous}$ does not change the trend of the $r_{Contact}$ changing with the elastic modulus E_{ML} of the multilayer film. The elastic modulus of amorphous MoS_2 will usually increase, after normal oxidation. Because there is currently no mature technological means to measure the elastic modulus of such a thin amorphous layer (~25 nm). Therefore, considering the strengthening effect of oxidation on the surface of the sample, we take 70 GPa, which is slightly higher than the elastic modulus of amorphous MoS_2 (experimental measurement values 45.84 ± 3.76 GPa) in the main text.

Table S1. The thicknesses of the metal and MoS_2 layers and the number of bilayer layers for MoS_2/Me multilayer films.

Sample	Thickness of MoS_2 layer (nm)	Thickness of Me layer (nm)	Bilayers of unirradiated films	Bilayers of irradiated films
MoS_2/Ti	29.7	6.0	49	48
MoS_2/Pb	30.5	8.5	49	48
MoS_2/Cu	29.3	6.6	49	48
MoS_2/W	29.9	5.7	49	48

Table S2. Statistical information of nanoparticles on the sliding interface of the MoS_2/W and MoS_2/W-AO multilayer films.

Sample	Number of particles in tribofilm	Total area of particles in tribofilm (nm^2)	Total area of tribofilm (nm^2)	Area ratio of particles to tribofilm
MoS_2/W	78	5743.5	61803.3	0.09
MoS_2/W-AO	286	6650.6	36230.4	0.18

Table S3. Deposition target current, elemental composition in cross-sections, and S/Mo of the as-prepared films.

Sample	Magnetic current (A), MoS_2	Magnetic current (A), Me	Composition (at.%)				S/Mo
			Mo	Me	S	O	
MoS_2/W	1.6	0.8	36.9	7.3	44.0	11.8	1.19
MoS_2/Ti	1.6	0.8	36.6	7.0	50.0	6.4	1.37
MoS_2/Pb	1.6	0.6	33.5	7.3	51.2	8.0	1.53
MoS_2/Cu	1.6	0.4	35.8	6.5	50.4	7.3	1.41
MoS_2/Ag	1.6	0.4	35.4	6.1	53.2	5.3	1.50

Table S4. System sizes, K-meshes, and the number of steps N for movement in the x, y, and z directions and corresponding distance L for each step in the calculation of interfacial friction.

Systems	K_x	K_y	K_z	a(Å)	b(Å)	c(Å)	α(°)	β(°)	γ(°)	N_x	N_y	N_z	L_x(Å)	L_y(Å)	L_z(Å)
MoS_2/MoS_2	7	7	1	3.14	3.14	32.01	90	90	120	6,	6	20	0.52	0.52	0.1
MoS_2/W	17	1	1	3.16	22.10	30.31	90	90	90	6	10	10	0.53	0.55	0.3
MoS_2/WO_3	1	3	1	15.55	5.36	32.99	90	90	90	10	10	7	0.31	0.353	0.25

Table S5. Lattice constants calculated from DFT as well as the corresponding K-meshes.

Systems	K_x	K_y	K_z	a(Å)	b(Å)	c(Å)	α(°)	β(°)	γ(°)
MoS_2	11	11	3	3.14	3.14	12.01	90	90	120
W	11	11	11	3.17	3.17	3.17	90	90	90
WO_3	5	5	4	5.27	5.13	7.62	90	92.25	90
Cu	11	11	11	3.64	3.64	3.64	90	90	90